

# Discrete unified gas kinetic scheme for the solution of electron Boltzmann transport equation with Callaway approximation

Meng Lian<sup>a</sup>, Chuang Zhang<sup>b</sup>, Zhaoli Guo<sup>c,\*</sup>, Jing-Tao Lü<sup>a,\*</sup>

<sup>a</sup>*School of Physics, Institute for Quantum Science and Engineering and Wuhan National High Magnetic Field Center, Huazhong University of Science and Technology, Wuhan 430074, China*

<sup>b</sup>*Department of Physics, Hangzhou Dianzi University, Hangzhou 310018, China*

<sup>c</sup>*Institute of Interdisciplinary Research for Mathematics and Applied Science, Huazhong University of Science and Technology, Wuhan 430074, China*

---

## Abstract

Electrons are the carriers of heat and electricity in materials, and exhibit abundant transport phenomena such as ballistic, diffusive, and hydrodynamic behaviors in systems with different sizes. The electron Boltzmann transport equation (eBTE) is a reliable model for describing electron transport, but it is a challenging problem to efficiently obtain the numerical solutions of eBTE within one unified scheme involving ballistic, hydrodynamics and/or diffusive regimes. In this work, a discrete unified gas kinetic scheme (DUGKS) in finite-volume framework is developed based on the eBTE with the Callaway relaxation model for electron transport. By reconstructing the distribution function at the cell interface, the processes of electron drift and scattering are coupled together within a single time step. Numerical tests demonstrate that the DUGKS can be adaptively applied to multiscale electron transport, across different regimes.

**Keywords:** Boltzmann transport equation, Discrete unified gas kinetic scheme, electron transport, Callaway Model

---

## 1. Introduction

With the development of nanoscience, microscale processing technologies, and advancements in nanoscale temperature measurement techniques, especially the continuous miniaturization and integration of chips, the carrier transport behavior of nano systems has become an important scientific issue in the statistical physics of nonequilibrium states [1–5]. For transport in metals and semiconductors, electrons play an important role and are characterized by rich transport phenomena, such as thermoelectric effect [6–8], hydrodynamics [9–11], and size effects [12]. As one of the widely used methods for studying electron transport, the electron Boltzmann equation (eBTE) can be used to solve problems over a large range of scales from the nanoscale to the macroscale [13]. The Callaway approximation [14] divides the scattering processes into two types. One conserves the total crystal momenta, while the other does not. It is able to successfully characterize transport behavior in the hydrodynamic regime [15, 16], which has received renewed interest in recent years, due to the experimental progress in graphene and other two-dimensional materials [17–19]. Development of multiscale and high accuracy method for solving eBTE under the Callaway approximation is highly desirable to further explore the complex characteristics of electron transport in realistic materials.

The numerical methods of eBTE are mainly divided into two types. One is to use macroscopic models to approximate the solution, such as the drift-diffusion model and the hydrodynamic equations [20–22]. These methods are simple in form, with high computational efficiency, and can accurately describe the electron transport behavior in large-scale devices. However, as the size of the device decreases, the electron mean free path is comparable to the characteristic length of the device. In such cases, the electron transport behavior exhibits quasi-ballistic or ballistic characteristics, rendering the aforementioned methods inaccurate. The other type is the direct numerical solution of

---

\*Corresponding author

Email addresses: zlguo@hust.edu.cn (Zhaoli Guo), jtl@hust.edu.cn (Jing-Tao Lü)

the eBTE, such as the Monte Carlo (MC) method, the discrete ordinates method (DOM) and the spherical harmonic expansion (SHE) method. The MC method uses random numbers to select the scattering mechanisms and determine the drift time under external field. It is very flexible and can be combined with the actual energy band structure to analyze the complex scattering process of the carriers. Currently, MC schemes have been developed for semiconductors [23] and metals [24], but are not suitable for weak external fields due to unavoidable statistical noise, i.e., it converges slowly at small Knudsen numbers due to decoupling of particle drift and scattering. The DOM method discretizes both real space and wavevector space, and solves the eBTE in the whole real space for each discretized wavevector [25, 26]. This method is suitable for systems with high Knudsen number, but exhibits significant numerical dissipation at small Knudsen number. The SHE method is widely used for the simulation of semiconductor devices [27–30]. By representing the electron distribution with spherical harmonic functions of a certain order, a series of equations are obtained, which can accurately describe the transport behavior of carriers. It is more advantageous than MC in weak external fields, and does not suffer from statistical noise. However, the numerical results depend on the order of the expansion, which needs to be taken care of in the high-field region. Meanwhile, the high computational complexity of SHE is challenging to simulate high-dimensional materials, which requires the use of matrix compression techniques [31]. In addition, the lattice Boltzmann methods (LBM) [32] have been applied to multiscale problems in nanosystems, but it may generate nonphysical solutions at high Knudsen numbers [33].

The finite-volume discrete unified gas kinetic scheme (DUGKS), which was originally developed for multiscale gas flows [34, 35], is a multiscale method with asymptotic preservation (AP) properties, and has been developed to address multiscale transport problems of other energy carriers. Actually, the DUGKS has been successfully applied in various fields such as multiscale gas flow, phonon heat transfer, radiative heat transfer, and plasma transport [36]. By coupling particle drift and scattering processes simultaneously in the flux reconstruction, this scheme allows the cell size and time step to be independent of the mean free path and relaxation time, and to recover adaptively from the ballistic limit to the diffusive limit [34, 35]. Very recently, some progress has been made in electron-phonon coupled heat transfer based on DUGKS [37]. However, it cannot be used to describe thermoelectric transport. Also, the single relaxation model used fails to capture the effects of electron momentum-conserving scattering.

In this study, we extend the application of DUGKS to study electrical, thermal and thermoelectric transport of electrons, incorporating the electronic band structure to iteratively solve for the temperature and chemical potential distributions. Numerical results are carefully compared to theoretical and numerical results. The advantage of DUGKS in solving multiscale problems is illustrated. The rest of the paper is organized as follows: Section 2 describes the electron Boltzmann equation, Section 3 details the DUGKS for the electron Boltzmann equation, Section 4 verifies the performance of the proposed DUGKS by simulating several typical problems, and conclusions are given in Section 5.

## 2. Electron Boltzmann transport equation

The Boltzmann transport equation describes the evolution of the quasi-particle distribution driven by external fields applied to the system. The transport properties can be readily calculated once the distribution function is known. The eBTE is expressed as:

$$\frac{\partial f}{\partial t} + \mathbf{v} \cdot \nabla_{\mathbf{r}} f + \dot{\mathbf{k}} \cdot \nabla_{\mathbf{k}} f = \left( \frac{\partial f}{\partial t} \right)_{\text{coll}}. \quad (1)$$

The distribution function  $f = f_n(\mathbf{r}, \mathbf{k}, t)$  depends on band index  $n$ , position  $\mathbf{r}$ , the wave vector  $\mathbf{k}$  and time  $t$ . Here we write it in an equivalent form  $f = f(\mathbf{r}, \varepsilon_n, s, t)$  where  $\varepsilon_n$  represents energy of the  $n$ -th band (in the following, for convenience of expression, we contract the band index  $n$ ,  $s$  represents the unit direction angle. For 3D case,  $s = (\cos \theta, \sin \theta \cos \varphi, \sin \theta \sin \varphi)$ , where  $\theta$  and  $\varphi$  are the polar and azimuthal angle. In 2D case, only  $\varphi$  is needed  $s = (\cos \varphi, \sin \varphi)$ . The group velocity of electrons depends on the band structure and is given by  $\mathbf{v} = \nabla_{\mathbf{k}} \varepsilon_n(\mathbf{k})/\hbar$ . The electric field  $\mathbf{E}$  determines the time derivative  $\dot{\mathbf{k}} = -e\mathbf{E}/\hbar$ . The right hand side presents the change of the distribution function due to electron collisions. It depends on the specific scattering mechanism, which can be expressed as

$$\left( \frac{\partial f}{\partial t} \right)_{\text{coll}} = - \int \frac{d\mathbf{k}'}{(2\pi)^3} \{ W(\mathbf{r}, \mathbf{k}, \mathbf{k}') f(\mathbf{k}) [1 - f(\mathbf{k}')] - W(\mathbf{k}', \mathbf{k}) f(\mathbf{k}') [1 - f(\mathbf{k})] \}, \quad (2)$$

where  $W(\mathbf{k}, \mathbf{k}')$  is the scattering kernel, which describes the rate of electron transition from state  $\mathbf{k}$  to  $\mathbf{k}'$ , and is usually obtained from the Fermi's golden rule.

The Boltzmann equation is a complicated nonlinear integral-differential equation which is difficult to solve even numerically. In this paper, we adopt the simplified Callaway approximation to describe the collision term, which is divided into two types, representing normal (N) and Umklapp (U) processes, respectively. The former fulfills crystal momentum conservation, while the latter does not due to the involved extra reciprocal lattice vector. A rich set of transport phenomena can be obtained from this simplified approximation, including ballistic, diffusive and hydrodynamic regimes.

Generally, the electric potential  $\varphi$  and the electric field  $\mathbf{E} = -\nabla\varphi$  needs to be obtained by solving the Poisson's equation. However, when the external field is relatively weak, the electric field can be represented by the gradient of the electrochemical potential, i.e.,  $\nabla\mu \approx -e\nabla\varphi$ . We use this approximation and avoid solving the Poisson equation [15, 16, 38]. The resulting eBTE can be written as

$$\frac{\partial f}{\partial t} + \mathbf{v} \cdot \nabla_{\mathbf{r}} f = \frac{f_0^U(T^U, \mu^U) - f}{\tau^U} + \frac{f_0^N(T^N, \mu^N, \mathbf{u}) - f}{\tau^N}. \quad (3)$$

Here,  $\tau^U$  and  $\tau^N$  are the relaxation times of U-process and N-process, respectively, and both depend on the electron state. The Fermi-Dirac distribution  $f_0^U$  and the shifted Fermi-Dirac distribution  $f_0^N$  with a common drift velocity  $\mathbf{u}$  for all electrons are given by:

$$f_0^U = \frac{1}{\exp[(\varepsilon - \mu^U)/k_B T^U] + 1}, \quad (4)$$

$$f_0^N = \frac{1}{\exp[(\varepsilon - \mu^N - \mathbf{p} \cdot \mathbf{u})/k_B T^N] + 1}. \quad (5)$$

The two sets of parameters  $\{\mu^U, T^U\}$  and  $\{\mu^N, T^N, \mathbf{u}\}$  in  $f_0^U$  and  $f_0^N$  are Lagrange multipliers in the maximum entropy principle, responsible for the conservation of particle number and energy in U-processes and the conservation of particle number, energy and momentum in N-processes, respectively. They are determined by the following equations

$$\int_{4\pi} \int_{-\infty}^{+\infty} \boldsymbol{\psi}^U \frac{D(\varepsilon)}{4\pi} \frac{f_0^U(T^U, \mu^U) - f}{\tau^U(\varepsilon)} d\varepsilon d\Omega = \mathbf{0}, \quad (6)$$

$$\int_{4\pi} \int_{-\infty}^{+\infty} \boldsymbol{\psi}^N \frac{D(\varepsilon)}{4\pi} \frac{f_0^N(T^N, \mu^N, \mathbf{u}) - f}{\tau^N(\varepsilon)} d\varepsilon d\Omega = \mathbf{0}, \quad (7)$$

where  $\boldsymbol{\psi}^U = (1, \varepsilon)^T$  and  $\boldsymbol{\psi}^N = (1, \varepsilon, \mathbf{p})^T$  denote the conserved quantities of the U-process and N-process, respectively,  $D(\varepsilon)$  is the electronic density of states,  $d\Omega$  is the differential of the direction angle. These equations can be used to get  $\{\mu^U, T^U\}$  and  $\{\mu^N, T^N, \mathbf{u}\}$ , once the nonequilibrium distribution function  $f$  is obtained.

The temporal parameters  $T^U$ ,  $T^N$ ,  $\mu^U$  and  $\mu^N$  with the dimensions of temperature and chemical potential can be different from the physical ones. On the other hand, the corresponding physical quantities  $\tilde{T}$  and  $\tilde{\mu}$  are determined from the local conservation laws,

$$\int_{-\infty}^{+\infty} \int_{4\pi} \frac{D(\varepsilon)}{4\pi} f_0(\tilde{T}_{loc}, \tilde{\mu}_{loc}) d\Omega d\varepsilon = \int_{-\infty}^{+\infty} \int_{4\pi} \frac{D(\varepsilon)}{4\pi} f d\Omega d\varepsilon, \quad (8)$$

$$\int_{-\infty}^{+\infty} \int_{4\pi} \varepsilon \frac{D(\varepsilon)}{4\pi} f_0(\tilde{T}_{loc}, \tilde{\mu}_{loc}) d\Omega d\varepsilon = \int_{-\infty}^{+\infty} \int_{4\pi} \varepsilon \frac{D(\varepsilon)}{4\pi} f d\Omega d\varepsilon. \quad (9)$$

It can be found that the distribution function  $f$  reduces to  $f^U$  and  $f^N$  in the diffusive and hydrodynamic regimes, respectively, while the intermediate regime it is a weighted average of the two. If  $\tau$  is constant,  $\tilde{T}$  and  $\tilde{\mu}$  calculated in the diffusive and hydrodynamic regions are the same as the spurious variables.

### 3. The discrete unified gas kinetic scheme

We introduce the DUGKS for solving Eq. (3) numerically. To facilitate the solution, we rewrite Eq. (3) with discrete angular space as

$$\frac{\partial f(\mathbf{r}, \varepsilon, \mathbf{s}_\alpha, t)}{\partial t} + \mathbf{v} \cdot \nabla_{\mathbf{r}} f(\mathbf{r}, \varepsilon, \mathbf{s}_\alpha, t) = \frac{f_0 - f(\mathbf{r}, \varepsilon, \mathbf{s}_\alpha, t)}{\tau}, \quad (10)$$

where  $f_0 = (\tau^N f_0^U + \tau^U f_0^N) / (\tau^N + \tau^U)$  and  $\tau = \tau^U \tau^N / (\tau^U + \tau^N)$ . In order to accurately evaluate the zeroth-order to second-order moments of the distribution function, the discrete angle  $\mathbf{s}_\alpha$  needs to satisfy the following requirements:

$$\sum_{\alpha} w_{\alpha} = \Omega, \quad \sum_{\alpha} w_{\alpha} \mathbf{s}_{\alpha} = \mathbf{0}, \quad \sum_{\alpha} w_{\alpha} \mathbf{s}_{\alpha} \mathbf{s}_{\alpha} = \frac{\Omega}{d} \mathbf{I}, \quad (11)$$

where  $w_{\alpha}$  is the weight of the angular discretization,  $d$  is the system dimension. For  $d = 2$ , we have  $\Omega = 2\pi$ ; for  $d = 3$ , we have  $\Omega = 4\pi$ , and  $\mathbf{I}$  is the corresponding unit matrix.

Similar to the calculation of phonon Boltzmann transport equation, we use the trapezoidal integration rule to discretize the energy space. For the direction angle space, the conventional  $S_N$  quadrature is not accurate enough for large Knudsen number and may have a serious "ray effect". To overcome these difficulties, we choose the Gauss-Legendre (G-L) rule to discretize the direction angle. The real space is discretized using the finite volume method, the mid-point rule is used for the time integration of the advection term, and the trapezoidal rule is used for the collision term. With these considerations, Eq. (3) is discretized as

$$f_{\alpha, \varepsilon, i}^{n+1} - f_{\alpha, \varepsilon, i}^n + \frac{\Delta t}{V_i} \mathbf{F}_{\alpha, \varepsilon, i}^{n+1/2} = \frac{\Delta t}{2} \left[ \frac{f_{0, \varepsilon, i}^{n+1} - f_{\alpha, \varepsilon, i}^{n+1}}{\tau_{\varepsilon}} + \frac{f_{0, \varepsilon, i}^n - f_{\alpha, \varepsilon, i}^n}{\tau_{\varepsilon}} \right], \quad (12)$$

where  $f_{\alpha, \varepsilon, i}^n$  denotes the cell-averaged occupation probability of electrons moving along the  $\mathbf{s}_{\alpha}$  direction in the cell  $i$  at the energy level  $\varepsilon$  at time  $t = n\Delta t$ ,  $V_i$  is the volume of cell  $i$  and  $\mathbf{F}_{\alpha, \varepsilon, i}^{n+1/2}$  is the flux across the interfaces of cell  $i$ , is expressed as

$$\mathbf{F}_{\alpha, \varepsilon, i}^{n+1/2} = \sum_{j \in \mathcal{N}_i} (\mathbf{v}_{\alpha, \varepsilon} \cdot \mathbf{n}_{ij}) f_{\alpha, \varepsilon}^{n+1/2}(\mathbf{x}_{ij}) S_{ij}, \quad (13)$$

where  $\mathcal{N}_i$  denotes the set of cells adjacent to cell  $i$ ,  $\mathbf{n}_{ij}$  is the unit normal vector pointing from cell  $i$  to cell  $j$ ,  $S_{ij}$  is the area of the interface  $ij$  between cells  $i$  and  $j$ , and  $f_{\alpha, \varepsilon}^{n+1/2}(\mathbf{x}_{ij})$  denotes the distribution function at the interface at the time of  $t_{n+1/2} = t_n + \Delta t/2$ . Two new distribution functions are introduced to remove the implicitness of Eq. (12)

$$\tilde{f}_{\alpha, \varepsilon, i}^n = f_{\alpha, \varepsilon, i}^n - \frac{\Delta t}{2} \left( \frac{f_{0, \varepsilon, i}^n - f_{\alpha, \varepsilon, i}^n}{\tau_{\varepsilon}} \right), \quad (14)$$

$$\tilde{f}_{\alpha, \varepsilon, i}^{+,n} = f_{\alpha, \varepsilon, i}^n + \frac{\Delta t}{2} \left( \frac{f_{0, \varepsilon, i}^n - f_{\alpha, \varepsilon, i}^n}{\tau_{\varepsilon}} \right). \quad (15)$$

Then, Eq. (12) can be rewritten as

$$\tilde{f}_{\alpha, \varepsilon, i}^{n+1} = \tilde{f}_{\alpha, \varepsilon, i}^{+,n} - \frac{\Delta t}{V_i} \mathbf{F}_{\alpha, \varepsilon, i}^{n+1/2}. \quad (16)$$

We can track the evolution of the distribution function  $\tilde{f}$  following Eq. (16), where the interface distribution function  $f_{ij}^{n+1/2}$  at half-time steps is reconstructed based on the eBTE, which is the key difference between the present DUGKS and classical DOM using certain direct numerical interpolations. First, along the characteristic line of Eq. (3) from time  $t_n$  to  $t_{n+1/2}$ , the end point  $\mathbf{x}_{ij}$  at the center of the interface between cell  $i$  and cell  $j$ .

$$f_{\alpha, \varepsilon}^{n+1/2}(\mathbf{x}_{ij}) - f_{\alpha, \varepsilon}^n(\mathbf{x}'_{ij}) = \frac{\Delta t}{4} \left[ \frac{f_{0, \varepsilon}^{n+1/2}(\mathbf{x}_{ij}) - f_{\alpha, \varepsilon}^{n+1/2}(\mathbf{x}_{ij})}{\tau_{\varepsilon}} + \frac{f_{0, \varepsilon}^n(\mathbf{x}'_{ij}) - f_{\alpha, \varepsilon}^n(\mathbf{x}'_{ij})}{\tau_{\varepsilon}} \right], \quad (17)$$

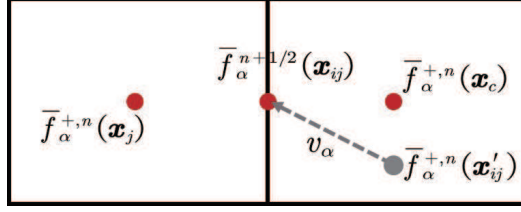


Figure 1: Schematic of reconstructed distribution function at the interface.

where  $\mathbf{x}'_{ij} = \mathbf{x}_{ij} - \mathbf{v}\Delta t/2$ . Again introducing two auxiliary distribution functions to remove the implicitness of Eq. (17)

$$\bar{f}_{\alpha,\varepsilon,i}^n = f_{\alpha,\varepsilon,i}^n - \frac{\Delta t}{4} \left( \frac{f_{0,\varepsilon,i}^n - f_{\alpha,\varepsilon,i}^n}{\tau_\varepsilon} \right), \quad (18)$$

$$\bar{f}_{\alpha,\varepsilon,i}^{+,n} = f_{\alpha,\varepsilon,i}^n + \frac{\Delta t}{4} \left( \frac{f_{0,\varepsilon,i}^n - f_{\alpha,\varepsilon,i}^n}{\tau_\varepsilon} \right), \quad (19)$$

it can be expressed as

$$\bar{f}_{\alpha,\varepsilon}^{n+1/2}(\mathbf{x}_{ij}) = \bar{f}_{\alpha,\varepsilon}^{+,n}(\mathbf{x}'_{ij}). \quad (20)$$

To evaluate the interface flux  $\mathbf{F}_{\alpha,\varepsilon,i}^{n+1/2}$ , we assume that the electron distribution function varies linearly in each cell to reconstruct the auxiliary function  $\bar{f}_{\alpha,\varepsilon}^{+,n}(\mathbf{x}'_{ij})$  in Eq. (20), as shown in Fig. 1, then

$$\bar{f}_{\alpha,\varepsilon}^{+,n}(\mathbf{x}'_{ij}) = \bar{f}_{\alpha,\varepsilon}^{+,n}(\mathbf{x}_c) + (\mathbf{x}'_{ij} - \mathbf{x}_c) \cdot \boldsymbol{\sigma}_c, \quad (21)$$

where  $\boldsymbol{\sigma}_c$  is the slope of the auxiliary function  $\bar{f}_{\alpha,\varepsilon}^{+,n}(\mathbf{x}'_{ij})$  in the cell where  $\mathbf{x}_c$  is located. We have  $c = i$  if  $\mathbf{v}_\alpha \cdot \mathbf{n}_{ij} > 0$  and  $c = j$  otherwise, which can be constructed smoothly by methods such as central-difference or van Leer limiter. In this work, we use the latter to construct the gradient to ensure numerical accuracy and stability. In 1D case, the van Leer limiter is defined as

$$\boldsymbol{\sigma}_i = [\text{sgn}(s_1) + \text{sgn}(s_2)] \frac{|s_1||s_2|}{|s_1| + |s_2|}, \quad (22)$$

where

$$s_1 = \frac{\bar{f}_{\alpha,\varepsilon,i}^{+,n} - \bar{f}_{\alpha,\varepsilon,i-1}^{+,n}}{x_i - x_{i-1}}, \quad s_2 = \frac{\bar{f}_{\alpha,\varepsilon,i+1}^{+,n} - \bar{f}_{\alpha,\varepsilon,i}^{+,n}}{x_{i+1} - x_i}. \quad (23)$$

As a result, the original distribution function  $f_{\alpha,\varepsilon}^{n+1/2}(\mathbf{x}_{ij})$  can be obtained from Eqs. (18), (20) and (21)

$$f_{\alpha,\varepsilon}^{n+1/2}(\mathbf{x}_{ij}) = \frac{4\tau}{4\tau + \Delta t} \bar{f}_{\alpha,\varepsilon}^{n+1/2}(\mathbf{x}_{ij}) + \frac{\Delta t}{4\tau + \Delta t} f_{0,\alpha,\varepsilon}^{n+1/2}(\mathbf{x}_{ij}), \quad (24)$$

where  $f_{0,\alpha,\varepsilon}^{n+1/2}(\mathbf{x}_{ij})$  is a function of  $\mu_{loc,ij}^{n+1/2}$  and  $T_{loc,ij}^{n+1/2}$ , which can be obtained by the particle number and energy conservation of the scattering operator. Since the original distribution function  $f$  in Eqs. (6) and (7) is unknown, the conservation equation needs to be converted to the form of  $\bar{f}$  from Eqs. (6), (7) and (18)

$$\int_{4\pi} \int_{-\infty}^{+\infty} \psi^U \frac{D(\varepsilon)}{4\pi} \left[ \frac{(4\tau^N + \Delta t) f_{0,ij}^{U,n+1/2} - \Delta t f_{0,ij}^{N,n+1/2}}{(4\tau + \Delta t)(\tau^U + \tau^N)} - \frac{4\tau \bar{f}_{ij}^{n+1/2}}{(4\tau + \Delta t)\tau^U} \right] d\varepsilon d\Omega = \mathbf{0}, \quad (25)$$

$$\int_{4\pi} \int_{-\infty}^{+\infty} \psi^N \frac{D(\varepsilon)}{4\pi} \left[ \frac{(4\tau^N + \Delta t) f_{0,ij}^{N,n+1/2} - \Delta t f_{0,ij}^{U,n+1/2}}{(4\tau + \Delta t)(\tau^U + \tau^N)} - \frac{4\tau \bar{f}_{ij}^{n+1/2}}{(4\tau + \Delta t)\tau^N} \right] d\varepsilon d\Omega = \mathbf{0}. \quad (26)$$

If multiple bands contribute to transport, the above equation should also include a summation over band indices. In this way, the interface flux  $\mathbf{F}_{\alpha,\varepsilon,i}^{n+1/2}$  is fully determined by Eqs. (13) and (24). From Eq. (16) we can obtain the distribution function  $\tilde{f}_{\alpha,\varepsilon,i}^{n+1}$  at  $t_{n+1}$ . Similarly,  $T_{loc,i}^{n+1}$  and  $\mu_{loc,i}^{n+1}$  can be determined from the following two equations

$$\int_{4\pi} \int_{-\infty}^{+\infty} \psi^U \frac{D(\varepsilon)}{4\pi} \left[ \frac{(2\tau^N + \Delta t) f_{0,i}^{U,n+1} - \Delta t f_{0,i}^{N,n+1}}{(2\tau + \Delta t)(\tau^U + \tau^N)} - \frac{2\tau \tilde{f}_i^{n+1}}{(2\tau + \Delta t)\tau^U} \right] d\varepsilon d\Omega = \mathbf{0}, \quad (27)$$

$$\int_{4\pi} \int_{-\infty}^{+\infty} \psi^N \frac{D(\varepsilon)}{4\pi} \left[ \frac{(2\tau^N + \Delta t) f_{0,i}^{N,n+1} - \Delta t f_{0,i}^{U,n+1}}{(2\tau + \Delta t)(\tau^U + \tau^N)} - \frac{2\tau \tilde{f}_i^{n+1}}{(2\tau + \Delta t)\tau^N} \right] d\varepsilon d\Omega = \mathbf{0}. \quad (28)$$

To solve Eqs. 25-28, we use the Newtonian iteration method. The electric and heat currents in the center of each cell can be expressed as

$$\mathbf{J}(\mathbf{x}_i, t) = -e \int_{4\pi} \int_{\varepsilon_{\min}}^{\varepsilon_{\max}} \mathbf{v} \frac{D(\varepsilon)}{4\pi} \frac{2\tau(\varepsilon)}{2\tau(\varepsilon) + \Delta t} \tilde{f}(\mathbf{x}_i, t) d\varepsilon d\Omega, \quad (29)$$

$$\mathbf{J}_q(\mathbf{x}_i, t) = \int_{4\pi} \int_{\varepsilon_{\min}}^{\varepsilon_{\max}} [\varepsilon - \tilde{\mu}(\mathbf{x}_i, t)] \mathbf{v} \frac{D(\varepsilon)}{4\pi} \frac{2\tau(\varepsilon)}{2\tau(\varepsilon) + \Delta t} \tilde{f}(\mathbf{x}_i, t) d\varepsilon d\Omega. \quad (30)$$

It is notable that the distribution functions  $\tilde{f}^+$ ,  $\tilde{f}^-$  and  $\tilde{f}$  satisfy the following relationship, which simplifies the calculation

$$\tilde{f}^- = \frac{4}{3}\tilde{f}^+ - \frac{1}{3}\tilde{f}. \quad (31)$$

Importantly, in DUGKS, the time step  $\Delta t$  is determined by the Courant-Friedrichs-Lewy (CFL) condition

$$\Delta t = \gamma \min\left(\frac{\Delta x}{v}\right), \quad (32)$$

where  $\gamma \in (0, 1)$  is the CFL number, such that the defined time step remains consistent for any relaxation time and has the AP property.

The procedure of the present DUGKS can be summarized as follows:

1. Set the initial temperature  $T_0$ , chemical potential  $\mu_0$ , discrete energy space, real space and direction angle space, and set the initial distribution function  $\tilde{f}_{\alpha,\varepsilon,i}^n$  according to Eq. (14);
2. Calculate  $\tilde{f}_{\alpha,\varepsilon,i}^{+,n}$  and its slope  $\sigma_c$ , and construct the distribution function  $\tilde{f}_{\alpha,\varepsilon}^{+,n}(\mathbf{x}'_{ij})$  according to Eq. (21);
3. Calculate the interface distribution  $\tilde{f}_{\alpha,\varepsilon}^{n+1/2}(\mathbf{x}_{ij})$  based on Eq. (22);
4. Calculate the local temperature  $T_{loc,ij}^{n+1/2}$  and local chemical potential  $\mu_{loc,ij}^{n+1/2}$  at the cell interface based on Eqs. (25) and (26) to obtain the corresponding equilibrium distribution  $f_{0,\alpha,\varepsilon}^{n+1/2}(\mathbf{x}_{ij})$ ;
5. Calculate the original distribution function  $f_{0,\alpha,\varepsilon}^{n+1/2}(\mathbf{x}_{ij})$  at the cell interface based on Eq. (24), and update the cell interface flux  $\mathbf{F}_{\alpha,\varepsilon,i}^{n+1/2}$  by Eq. (13);
6. Calculate  $\tilde{f}_{\alpha,\varepsilon,i}^{+,n}$  based on Eq. (31) to update  $\tilde{f}_{\alpha,\varepsilon,i}^{n+1}$  at the new time step by Eq. (16);
7. Update the temperature  $T_{loc,i}^{n+1}$  and chemical potential  $\mu_{loc,i}^{n+1}$  of the cell at the next time step based on Eqs. (27) and (28);
8. Repeat step 2 to step 8 until stop criterion is reached.

### 3.1. Boundary conditions

For isothermal boundary conditions, electrons colliding with the boundary are absorbed, while an electron in equilibrium at the boundary temperature  $T_b$  and chemical potential  $\mu_b$  is emitted into the computational domain,

$$f(\mathbf{x}_b, \varepsilon, \mathbf{s}) = f_0(T_b, \mu_b, \varepsilon), \quad \mathbf{s} \cdot \mathbf{n}_b > 0 \quad (33)$$

where  $\mathbf{n}_b > 0$  is the unit normal vector pointing from the interface to the domain.

For periodic boundary conditions, driven by temperature and/or chemical potential gradient, an electron leaves one boundary while another electron with the same velocity and energy enters the domain from the corresponding periodic boundary. The distribution of these two electrons deviates equally from the equilibrium state at the passing boundary,

$$f(\mathbf{x}_{b1}, \varepsilon, \mathbf{s}) - f_0(T_{b1}, \mu_{b1}, \varepsilon) = f(\mathbf{x}_{b2}, \varepsilon, \mathbf{s}) - f_0(T_{b2}, \mu_{b2}, \varepsilon) \quad (34)$$

where  $b1$  and  $b2$  denote the corresponding periodic boundaries, respectively.

For diffusive reflection boundary, it is assumed that electrons reflected from the boundary are isotropic

$$f(\mathbf{x}_b, \varepsilon, \mathbf{s}) = \frac{\int_{\mathbf{s}' \cdot \mathbf{n}_b < 0} (\mathbf{s}' \cdot \mathbf{n}_b) f(\mathbf{x}_b, \varepsilon, \mathbf{s}') d\Omega}{\int_{\mathbf{s}' \cdot \mathbf{n}_b > 0} \mathbf{s}' \cdot \mathbf{n}_b d\Omega}, \quad \mathbf{s} \cdot \mathbf{n}_b > 0. \quad (35)$$

Meanwhile, for specular reflection boundary, we have

$$f(\mathbf{x}_b, \varepsilon, \mathbf{s}) = f(\mathbf{x}_b, \varepsilon, \mathbf{s}''), \quad \mathbf{s} \cdot \mathbf{n}_b > 0 \quad (36)$$

where  $\mathbf{s}'' = \mathbf{s} - 2(\mathbf{s} \cdot \mathbf{n}_b) \mathbf{n}_b$ . It is noted that both diffusive and specular boundaries no energy and particle exchanges occur at the interface, and are therefore also called adiabatic boundaries.

#### 4. Numerical results

In this section, numerical calculation of four types of problems are performed to test the performance of DUGKS. For the first two examples, we consider the cross-plane (Subsec. 4.1) and in-plane (Subsec. 4.2) electron transport of the Au films to verify the DUGKS solution against the deviational MC scheme available in the literature [24]. In the third example (Subsec. 4.3), we consider hydrodynamic transport in 2D systems using parameters of graphene. In the last example (Subsec. 4.4), we consider quasi-1D thermoelectric transport in model metal and semiconductor systems.

In all calculations, we take into account electrons in the energy window of  $[\mu_+ + 15k_B T_0, \mu_- - 15k_B T_0]$ , with  $\mu_+$  and  $\mu_-$  the higher and lower chemical potential, respectively. The energy window is uniformly discretized. The grid number is denoted as  $N_\varepsilon$ . In the direction angle space,  $\theta$  and  $\varphi$  are discretized into  $N_\theta$  and  $N_\varphi$  subdirections using G-L rule.

Note that if real physical quantities are used in the computation, large round off errors may occur due to the large disparity of their magnitudes. Therefore, dimensionless quantities are employed in our computation, where the following non-dimensional variables are employed,

$$\begin{aligned} \varepsilon^* &= \frac{\varepsilon}{\varepsilon_F}, \quad \mu^* = \frac{\mu}{\varepsilon_F}, \quad T^* = \frac{T}{T_0}, \quad \mathbf{p}^* = \frac{\mathbf{p}}{\hbar k_F}, \quad \mathbf{u}^* = \frac{\hbar k_F}{\varepsilon_F} \mathbf{u}, \\ \mathbf{r}^* &= \frac{\mathbf{r}}{L_{ref}}, \quad t^* = \frac{v_F t}{L_{ref}}, \quad \mathbf{v}^* = \frac{\mathbf{v}}{v_F}, \quad \text{Kn}^U = \frac{v_F \tau^U}{L_{ref}}, \quad \text{Kn}^N = \frac{v_F \tau^N}{L_{ref}}, \end{aligned}$$

where \* denotes that the quantity is dimensionless (omitted in the text for ease of presentation),  $\text{Kn}^U$  and  $\text{Kn}^N$  are the Knussen numbers of the U-process and the N-process,  $\varepsilon_F$ ,  $k_F$ , and  $v_F$  are the Fermi energy, Fermi wavevector, and Fermi velocity, respectively, and  $L_{ref}$  is the characteristic length.

##### 4.1. Cross-plane electron thermal transport

The reciprocal lattice of Au is of bcc type, and the first Brillouin zone is a truncated octahedron. The Fermi surface, although distorted along the  $\langle 111 \rangle$  direction, is approximately spherical, so we use the nearly-free electron model  $\varepsilon = \hbar^2 \mathbf{k}^2 / (2m)$  and set the Fermi energy  $\varepsilon_F = 5.51$  eV. To compare with the analytical results, we focus only on the U-processes and set  $\tau^U = 27.7 \sqrt{\varepsilon / \varepsilon_F}$  fs,  $\tau^N \rightarrow \infty$ . The CFL number is fixed at 0.7. The average temperature  $T_0$  is set to 300K.

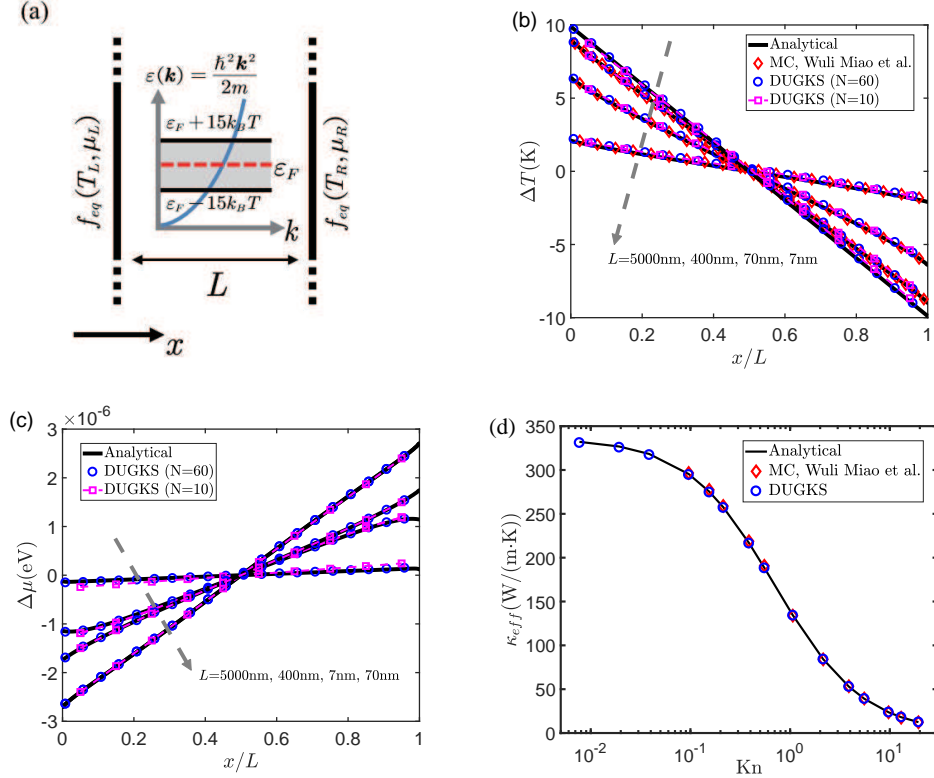


Figure 2: Cross-plane electron thermal transport in Au films. (a) Schematic of the system setup. The energy band structure is shown in the middle. The gray area is the energy range considered in the calculation. We choose  $\Delta T_L = -\Delta T_R = 10$  K without initial chemical potential difference. (b) steady-state temperature distribution; (c) steady-state chemical potential distribution; (d) variation of effective thermal conductivity with Knudsen number.

We first consider the cross-plane ( $x$  direction) electron thermal transport. The structure is shown in Fig. 2a. This is a quasi-1D problem since the system is translational invariant in  $y$  and  $z$  directions. We use isothermal boundary condition with  $T_L = T_0 + \Delta T_L$ ,  $T_R = T_0 + \Delta T_R$ . When  $\Delta T_L$  and  $\Delta T_R$  are relatively small, the distribution function can be linearized as  $f \approx C_T \Delta T + C_\mu \Delta \mu$ , with  $C_T = \partial f_0 / \partial T$  and  $C_\mu = \partial f_0 / \partial \mu$ . A semi-analytical solution can then be obtained using the linear approximation, following Ref. [39],

$$2 \int_{\varepsilon_{\min}}^{\varepsilon_{\max}} \frac{D(\varepsilon)}{\tau(\varepsilon)} \begin{pmatrix} \varepsilon C_T & \varepsilon C_\mu \\ C_T & C_\mu \end{pmatrix} d\varepsilon \cdot \begin{pmatrix} \Delta T(\hat{x}) \\ \Delta \mu(\hat{x}) \end{pmatrix} = F(\hat{x}) + \int_0^1 K(\hat{x}, \hat{x}') \begin{pmatrix} \Delta T(\hat{x}') \\ \Delta \mu(\hat{x}') \end{pmatrix} d\hat{x}'. \quad (37)$$

This is the second type of Fredholm integral equation, with  $\hat{x} = x/L$  the dimensionless coordinate, and

$$F(\hat{x}) = \int_{\varepsilon_{\min}}^{\varepsilon_{\max}} \frac{D(\varepsilon)}{\tau(\varepsilon)} \begin{pmatrix} \varepsilon C_T & \varepsilon C_\mu \\ C_T & C_\mu \end{pmatrix} \left[ E_2 \left( \frac{\hat{x}}{Kn_\varepsilon} \right) \begin{pmatrix} \Delta T_L \\ \Delta \mu_L \end{pmatrix} + E_2 \left( \frac{1-\hat{x}}{Kn_\varepsilon} \right) \begin{pmatrix} \Delta T_R \\ \Delta \mu_R \end{pmatrix} \right] d\varepsilon, \quad (38)$$

$$K(\hat{x}, \hat{x}') = \int_{\varepsilon_{\min}}^{\varepsilon_{\max}} \frac{D(\varepsilon)}{Kn_\varepsilon \tau(\varepsilon)} E_1 \left( \frac{|\hat{x} - \hat{x}'|}{Kn_\varepsilon} \right) \begin{pmatrix} \varepsilon C_T & \varepsilon C_\mu \\ C_T & C_\mu \end{pmatrix} d\varepsilon. \quad (39)$$

Here,  $E_n(x) = \int_0^1 \theta^{n-2} \exp(-x/\theta) d\theta$ , and  $Kn_\varepsilon = v_\varepsilon \tau_\varepsilon / L$  is the energy-dependent Knudsen number. From the above equations, we can obtain  $\Delta T(\hat{x})$  and  $\Delta \mu(\hat{x})$  using the degenerate kernels method.

We can then calculate the steady-state heat flux density as

$$J_q = \int \int_0^1 (\varepsilon - \varepsilon_F) f^+ v \theta d\theta d\varepsilon - \int \int_0^1 (\varepsilon - \varepsilon_F) f^- v \theta d\theta d\varepsilon, \quad (40)$$



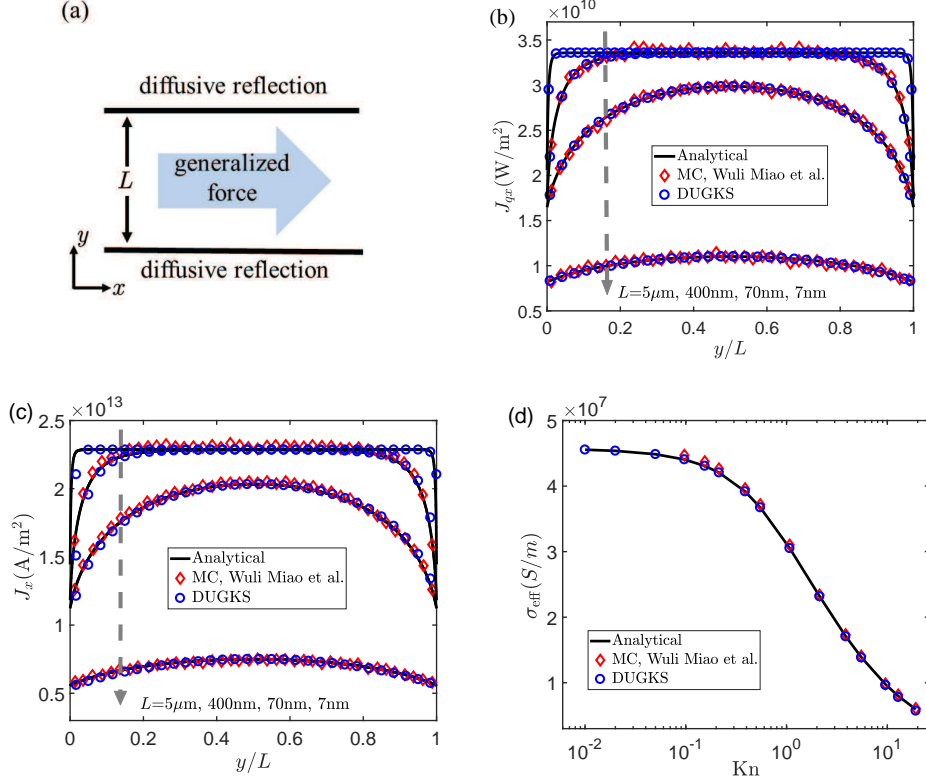


Figure 3: In-plane electrical and thermal transport in Au films, with  $L = 5 \mu\text{m}, 400 \text{ nm}, 70 \text{ nm}, 7 \text{ nm}$ , covering both diffusive and ballistic transport regimes. The real space grids are set to  $N_x \times N_y = 2 \times 60$ , and the direction angle grids are  $N_\theta \times N_\varphi = 40 \times 40$ . (a) Schematic of the transport setup. (b) Heat flux density ( $J_{qx}$ ) distribution along  $y$  driven by temperature gradient in  $x$  direction. (c) Current density ( $J_x$ ) distribution along  $y$  driven by a chemical potential gradient in  $x$  direction. (d) The effective conductivity  $\sigma_{\text{eff}} = e\bar{J}_x / (d\mu/dx)$  as a function of Knudsen number. Here,  $\bar{J}_x$  is the average of  $J_x$  along  $y$ .

where  $f^+$  and  $f^-$  describe the forward and backward transport of electrons, respectively, and can be written as

$$f^+(\hat{x}) = (C_T \Delta T_L + C_\mu \Delta \mu_L) e^{-\frac{\hat{x}}{Kn_e \theta}} + \int_0^{\hat{x}} \frac{C_T \Delta T(\hat{x}') + C_\mu \Delta \mu(\hat{x}')}{Kn_e \theta} e^{\frac{\hat{x}' - \hat{x}}{Kn_e \theta}} d\hat{x}', \quad (41)$$

$$f^-(\hat{x}) = (C_T \Delta T_R + C_\mu \Delta \mu_R) e^{-\frac{1-\hat{x}}{Kn_e \theta}} + \int_{\hat{x}}^1 \frac{C_T \Delta T(\hat{x}') + C_\mu \Delta \mu(\hat{x}')}{Kn_e \theta} e^{\frac{\hat{x}' - \hat{x}}{Kn_e \theta}} d\hat{x}'. \quad (42)$$

The effective thermal conductivity of the system is then obtained from

$$\kappa_{eff} = L J_q / |T_L - T_R|. \quad (43)$$

Different transport regimes can be characterized by the Knudsen number  $\text{Kn} = \lambda / L_{\text{ref}}$ , where  $\lambda$  is the electron mean free path. When  $\text{Kn} \ll 1$ , electrons are frequently scattered and exhibit diffusive transport; when  $\text{Kn} \gg 1$ , they move through the material almost without scattering and exhibit ballistic transport. We consider several different lengths  $L = 5 \mu\text{m}, 400 \text{ nm}, 70 \text{ nm}, 7 \text{ nm}$ . The corresponding  $\text{Kn}$  is 0.0077, 0.096, 0.55, 5.5, respectively, going from diffusive to ballistic regime. We compare our numerical results with the above semi-analytical solution and deviational MC results [24]. The direction angle is discretized into  $N_\theta = 100$  sub-directions using the G-L rule, and the system in  $x$  direction is uniformly discretized to  $N = 60$  and 10, respectively. The results are shown in Figs. 2b-2d. Fig. 2b shows that as the film size decreases, the system deviates from Fourier's law, and the boundary temperature slip becomes significant. As the mean free path of electrons increases, the electrons moving to the boundary are not sufficiently thermalized and strongly scatter with the electrons emitted from the boundary, giving rise to a nonlinear

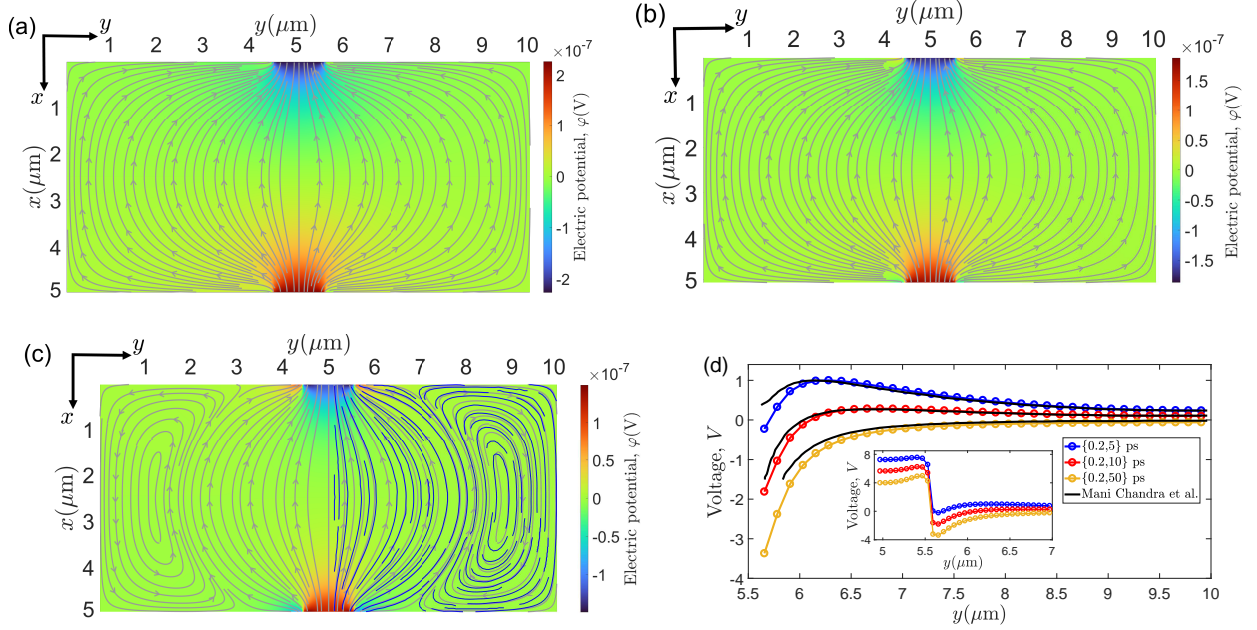


Figure 4: DC and AC hydrodynamic transport in 2D sheet of size  $5 \times 10 \mu\text{m}$ . We use  $N_e = 80$ ,  $N_x \times N_y = 80 \times 160$  for energy and real space, respectively. For 2D angle space, we use  $N_\phi = 400$ . Potential distribution and current lines for  $\{\tau^N, \tau^U\} =$  (a)  $\{0.2, 5\}$  ps, (b)  $\{0.2, 10\}$  ps, (c)  $\{0.2, 50\}$  ps, and the darker line in (c) is the result of Mani Chandra *et al.* (d) The potential difference between lower and upper boundary at  $y \in [5.5, 10] \mu\text{m}$ . We scaled results for other cases by setting the maximum value from parameter set  $\{0.2, 5\}$  ps to 1. The subplot shows the potential distribution at  $y \in [5.5, 7] \mu\text{m}$ , where the jump in value can be observed.

temperature distribution. Our scheme also captures the temperature-induced change in chemical potential (Fig. 2c), caused by the thermoelectric effect. For small temperature difference, this change is so tiny that we can ignore it when considering electron thermal transport. However, this small change is an essential factor in maintaining particle number conservation. The behavior of the effective thermal conductivity (Fig. 2d) is similar to that of the phonon case, with enhanced boundary scattering suppressing the thermal conductivity as the film thickness decreases.

Thus, we find good agreement of our numerical results with the analytical solutions in the whole range from ballistic to diffusive transport, with good convergence on multiscale. Due to the coupled treatment of drift and scattering, in our scheme the mesh size does not have to be smaller than the particle mean free path. The results converge well even for sparse meshes with  $N = 10$ . In addition, the time step  $\Delta t$  is completely determined by the CFL number and is not constrained by the relaxation time. These illustrate that the scheme has AP property.

#### 4.2. In-plane electron transport

In this subsection, as an example of quasi-2D transport, we calculate the in-plane thermal and electrical transport properties in Au thin films. The system setup is shown in Fig. 3a. We use the diffusive boundaries for the upper and lower sides, and periodic boundaries for the left and right sides. Due to the applied generalized forces (e.g., temperature or chemical potential gradient), the distribution function deviates from the equilibrium one and is written as  $f = f_0 + f_1$ , with  $f_0$  the equilibrium part, and  $f_1$  a small deviation. It can be described by the Fuchs-Sondheimer theory [40, 41]:

$$f_1 = \begin{cases} -v_y \tau \left( \frac{\partial f_0}{\partial T} \frac{dT}{dy} + \frac{\partial f_0}{\partial \mu} \frac{d\mu}{dy} \right) \left[ 1 - \exp\left(-\frac{x}{\tau v_x}\right) \right], & v_x > 0 \\ -v_y \tau \left( \frac{\partial f_0}{\partial T} \frac{dT}{dy} + \frac{\partial f_0}{\partial \mu} \frac{d\mu}{dy} \right) \left[ 1 - \exp\left(\frac{L-x}{\tau v_x}\right) \right], & v_x < 0 \end{cases} \quad (44)$$

The electrical and heat flux density can be calculated from  $f_1$ .

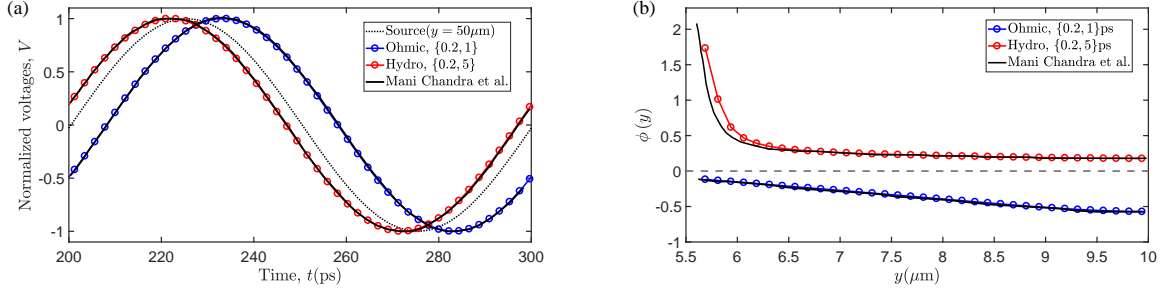


Figure 5: (a) Change in normalized potential at  $y = 90 \mu\text{m}$  from  $t = 200$  ps to  $t = 300$  ps; (b) Phase difference of the potential waveform at  $y \in [5.7, 10] \mu\text{m}$  with respect to  $y = 50 \mu\text{m}$  (i.e., the source current).

We consider the temperature and chemical potential driven cases separately. The results for temperature-driven case with  $dT/dx = -0.1$  K/nm are shown in Fig. 3b. This scheme again accurately captures the heat transfer process at different Knudsen numbers. In contrast to MC, the DUGKS results are free from random errors, and the mean free path does not limit the mesh size. The heat flux density saturates at  $L = 5 \mu\text{m}$ , corresponding to diffusive transport, following Fourier's law. The suppression of heat flux at the boundaries is due to inelastic scattering occurring at the diffusive reflection boundary. The heat flux density distribution becomes uniform again in the ballistic regime. For chemical-potential-driven case, with  $d\mu/dx = -e\nabla\varphi$ ,  $-\nabla\varphi = 5 \times 10^5$  V/m, the results are shown in Figs. 3c-3d. The agreement with analytical solutions again demonstrates the accuracy of this multiscale scheme.

### 4.3. DC and AC hydrodynamic transport

In this subsection, we calculate DC and AC electronic transport in a 2D sheet, using parameters of graphene. Assuming heavy  $n$  type doping, we consider only the contribution from the upper band with the linear dispersion relation of  $\varepsilon(k) = \hbar v_F k$ , where  $v_F \approx 10^6$  m/s is the Fermi velocity. Since hydrodynamic transport takes place at relative low temperatures, we set  $T_0 = 10$  K,  $\mu_0 = 10.8$  meV. We assume that DC and AC drive locate at the center of left and right boundaries with width of  $1 \mu\text{m}$ . We adopt the same boundary conditions as Ref. [15]. Specifically, for DC calculations, we set an isothermal boundary for the drift velocity  $u_{x0}^L = u_{x0}^R = 10^{-4} v_F$  distributed at the injections, and for AC calculations, we set an isothermal boundary for  $u_{x0}^L = u_{x0}^R = 10^{-4} v_F \sin(2\pi f t)$ , where  $f = 10$  GHz is the frequency of AC driving. For the other boundaries, we use specular reflection. For such problems, one is often interested in the voltage or potential of the system. In our framework, we can obtain the potential by  $\varphi(\mathbf{r}, t) = -\mu(\mathbf{r}, t)/e + \mu_0/e$ . We calculated the hydrodynamic transport dominated by the N-processes for the three cases with  $\{\tau^N, \tau^U\} = \{0.2, 5\}$  ps,  $\{0.2, 10\}$  ps and  $\{0.2, 50\}$  ps, respectively. The results are shown in Figs. 4a-4c. Although all three sets of relaxation times are dominated by N-processes, only results from the third parameter set shows vortices. Positions of the vortices are consistent with the results of Mani *et al.* [15] and nonlocal negative resistance is also observed (Fig. 4d).

For AC transport, we have considered two sets of parameters  $\{0.2, 1\}$  ps and  $\{0.2, 5\}$  ps. DUGKS again accurately captures the voltage transients (Fig. 5a). Fig. 5b shows that, for the Ohmic transport, the phase  $\phi(y) = \phi[I_d, \varphi(y)]$  follows the source current at any position, but for the hydrodynamic transport it consistently delayed from the source current.

### 4.4. Thermoelectric transport

In this subsection, we consider thermoelectric transport in model metals and semiconductors with  $L = 200$  nm. The left and right chemical potentials are set to  $\mu_L = \varepsilon_F + \Delta\mu/2$  and  $\mu_R = \varepsilon_F - \Delta\mu/2$ , where  $\Delta\mu$  is 10 meV, 20 meV, and 40 meV, respectively. For semiconductors, we use the effective mass approximation  $\varepsilon = \hbar^2 k^2 / 2m^*$ , with  $m^*$  the electron effective mass. We assume that the semiconductor is isotropic,  $n$  doped with a conduction band effective mass  $m^* = 0.068m$ . The Fermi energy level is located  $\Delta = 0.05$  eV below the conduction band bottom. For both metal and semiconductor, the energy, real and angle space grids are set to  $N_\varepsilon = 80$ ,  $N = 80$ ,  $N_\theta = 100$ , respectively. We considered both U ( $\tau^U = 0.01$  ps,  $\tau^N = 1$  s) and N ( $\tau^U = 1$  s,  $\tau^N = 0.01$  ps) dominated cases.

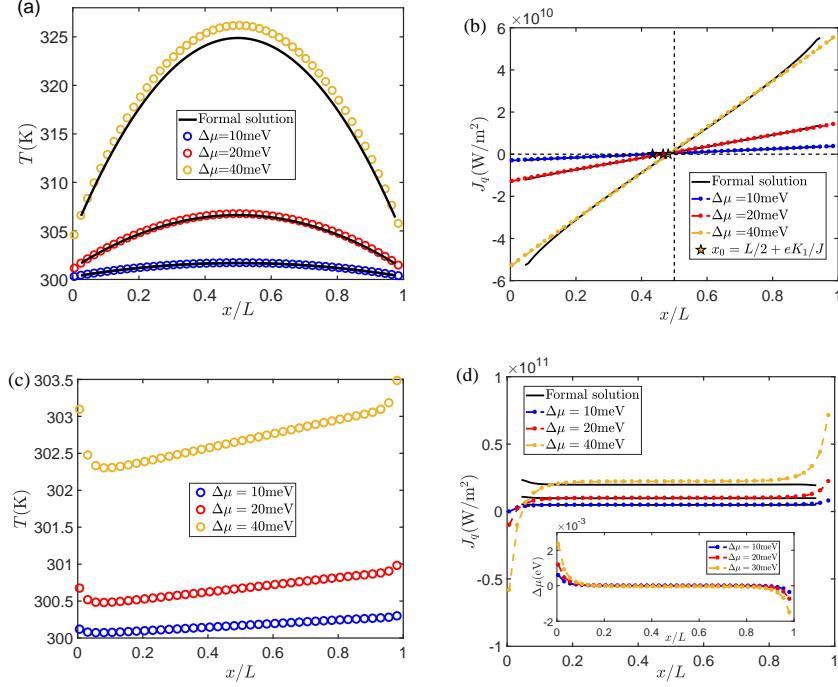


Figure 6: Numerical results for metal. (a) Temperature distribution due to chemical potential difference for the U-process-dominated case. (b) The corresponding heat flux density distribution for the situation in (a). (c) Temperature distribution due to chemical potential difference in the N-process-dominated case. (d) The corresponding heat flux density distribution for the situation in (c). The inset shows the corresponding chemical potential distribution.

Although there is no analytical solution, we can interpret the results qualitatively using a first-order approximation of the eBTE. With the U-processes dominating, it is described as:

$$\begin{pmatrix} \mathbf{J} \\ \mathbf{J}_q \end{pmatrix} = \begin{pmatrix} eK_0 & -eK_1/T \\ -K_1 & K_2/T \end{pmatrix} \begin{pmatrix} \nabla\mu \\ -\nabla T \end{pmatrix}, \quad (45)$$

and

$$K_n = \frac{\tau}{3} \iint v v D(\varepsilon) (\varepsilon - \mu)^n \left( -\frac{\partial f_0}{\partial \varepsilon} \right) d\varepsilon d\Omega. \quad (46)$$

In fact, Eq. 45 neglects the impact of boundary conditions, making it valid only in regions far from the boundaries [42]. Thus, we describe the region of  $x \in [5, 195]$  nm by Eq. 45.

The results for the metal in the U-process-dominated case are shown in Figs. 6a-6b. The temperature distribution takes the form of a quadratic function, with the peak occurring at  $L/2$ . This is expected when Joule heating is dominated [43]. In this case, using Eq. 45, we can obtain a formal solution for the  $T(x)$ :

$$T(x) = -\frac{\bar{T}}{K_2} \frac{d\mu}{dx} \left( \frac{J}{e} x^2 - \frac{J}{e} x_0 x + K_1 x \right) + T_0 + \Delta T_C, \quad (47)$$

where  $\Delta T_C$  is the temperature jump due to the thermal resistance of the interface, and  $x_0$  is the zero point of heat flux. We neglect the spatial dependence of  $K_n$  in obtaining Eq. 47, and assume that the chemical potential is linearly distributed. For metal, this applies away from the boundary. The results are shown in Fig. 6a, which agree well with the numerical results at low chemical potential differences. When  $\Delta\mu = 40\text{meV}$ , the large magnitude of the temperature change invalidates the above simple approximation. Now we consider the heat flux density in Fig. 6b. We note the small deviation of  $x_0$  at  $L/2 + eK_1/J$  from  $L/2$ , due to the thermoelectric correction term  $eK_1/J$ . As the chemical potential difference increases, the zero point shifts towards the center due to the increase in the current

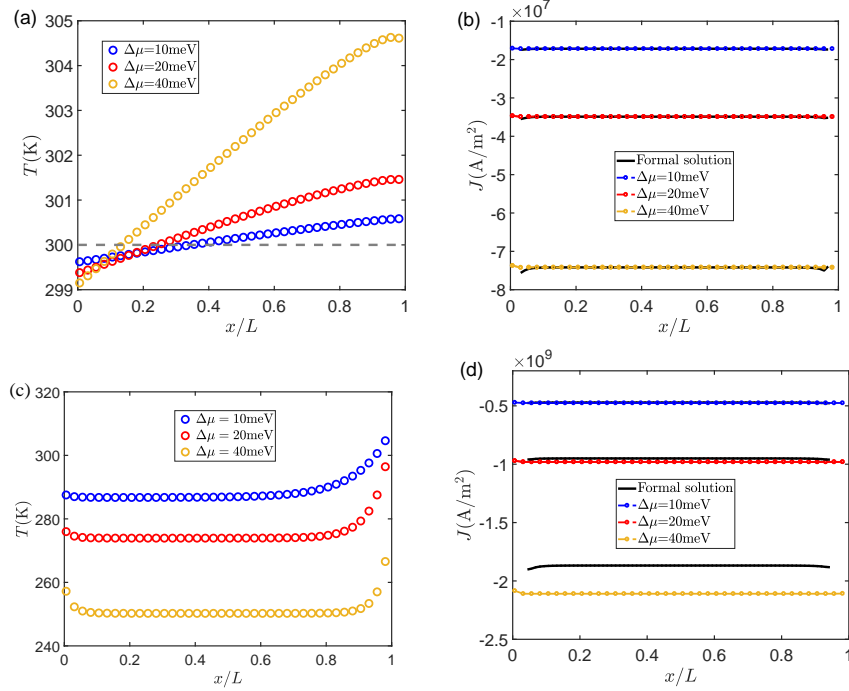


Figure 7: Numerical results for semiconductor. (a) Temperature distribution due to chemical potential difference when the U-processes dominate. (b) The corresponding current density distribution for the situation in (a). (c) Temperature distribution in semiconductors due to chemical potential difference when the N-processes dominate. (d) The corresponding current density distribution for the situation in (c).

density. For  $\Delta\mu = 40$  meV, the effect of the boundary conditions on the results is enhanced, leading to a deviation of the heat flux density close to the boundary.

The results for the metal when N-process dominates are shown in Figs. 6c-6d. The presence of drift velocity  $\mathbf{u}$  further complicates the results. Since the momentum conservation of the N-process does not generate thermal resistance, the temperature distribution should be homogeneous. However, the presence of boundary scattering makes the temperature non-uniform (See Fig. 6c). The electrons carry heat in from left boundary and do not dissipate heat in the middle. Eventually the electrons are scattered and release heat at the right boundary, resulting in higher temperatures on the right side than on the left. This non-uniformity becomes evident with the increase of the chemical potential difference. In addition, the temperature increase produced by the N-process is much lower than that of the U-process for the same chemical potential difference. The results of the heat flux are shown in Fig. 6d. They can be understood from the first-order approximation:

$$\begin{pmatrix} J \\ J_q \end{pmatrix} = \frac{1}{3} \iint D(\varepsilon) \begin{pmatrix} -e \\ \varepsilon - \mu \end{pmatrix} \mathbf{v} \cdot \frac{\partial f_0^N}{\partial \mathbf{u}} \Big|_{\mathbf{u}=0} d\varepsilon d\Omega \mathbf{u} + \begin{pmatrix} eK_0 & -eK_1/T \\ -K_1 & K_2/T \end{pmatrix} \begin{pmatrix} \nabla\mu \\ -\nabla T \end{pmatrix}, \quad (48)$$

where the first term on the right side is the effect of drift velocity. Since the temperature and chemical potential gradient are small, the contributions to the current and heat flux in the N-process come mainly from  $\mathbf{u}$ . The heat flux generated by the drift velocity term is nearly two orders of magnitude higher than the contributions from the temperature and the chemical potential. As in the previous analysis, momentum conservation makes the heat flux gradient zero in the region away from the boundary. The heat flux can also be written as  $\mathbf{J}_q = \mathbf{J}_\varepsilon - \mu\mathbf{J}$ , which satisfies  $\nabla\mathbf{J}_\varepsilon = 0$  and  $\nabla\mathbf{J} = 0$  at the steady state. This implies that the deviation of the heat flux from the first-order approximation arises mainly from the effect of boundary scattering on the chemical potential (See the inset of Fig. 6d).

Results for semiconductor model are depicted in Fig. 7. The temperature distribution when U-processes dominate is shown in Fig. 7a. Unlike metals, cooling takes place at the left boundary and becomes more apparent as the chemical potential difference increases. This is characteristic of the Peltier effect. The Peltier coefficient is defined

as  $\Pi = K_1 / (eK_0)$ . From the numerical data, we get an average value of  $\Pi = 0.1$  V. Fig. 7b shows the corresponding current densities, which are consistent with Eq. 45. For the case where N-processes dominate (Fig. 7c, 7d), the conservation of momentum during the collision leads to the uniform decrease of temperature in the region away from the boundary. This cooling phenomenon is more pronounced compared to the U-process (Fig. 7c). The corresponding average Peltier coefficient is  $\Pi = 0.09$  V, similar to the U-dominated case. However, the temperature decreases much more since the current density  $|J|$  is two orders of magnitude larger than the case where the U-processes dominate (See Fig. 7b and 7d). The first-order approximation no longer holds as  $\Delta\mu$  increases to 40 meV.

## 5. Conclusion

In summary, we developed a discrete unified gas kinetic scheme for the solution of electron Boltzmann transport equation under Callaway approximation. The coupled treatment of electron drift and scattering makes the cell size and time step independent of the mean free path and relaxation time, which has advantage in the study of problems with small Knudsen number. Numerical results demonstrate that the scheme accurately captures electron transport behaviors across ballistic, hydrodynamic, and diffusive regimes, while also exhibiting asymptotic preservation properties. Due to the consideration of the electronic energy band structure and the use of the Newtonian method to solve the energy and particle number conservation equations at the cell interfaces and centers, we are able to simulate different materials across a wide range of parameter regimes. Meanwhile, more complex device shapes, more realistic energy band structure can also be incorporated into our framework in the future. Study of coupled transport including more than one type of quasiparticles, i.e., including photon-electron-phonon coupled system, is also possible under this generic scheme. However, the dynamics of electrons in  $k$ -space needs to be included to study transport under strong electric and magnetic fields. This issue will be discussed in the future.

## References

- [1] D. G. Cahill, P. V. Braun, G. Chen, D. R. Clarke, S. Fan, K. E. Goodson, P. Koblinski, W. P. King, G. D. Mahan, A. Majumdar, H. J. Maris, S. R. Phillpot, E. Pop, L. Shi, Nanoscale thermal transport. II. 2003–2012, *Appl. Phys. Rev.* 1 (1) (2014) 011305. doi:10.1063/1.4832615.
- [2] D. G. Cahill, W. K. Ford, K. E. Goodson, G. D. Mahan, A. Majumdar, H. J. Maris, R. Merlin, S. R. Phillpot, Nanoscale thermal transport, *J. Appl. Phys.* 93 (2) (2003) 793–818. doi:10.1063/1.1524305.
- [3] S. J. Pearton, F. Ren, M. Tadjer, J. Kim, Perspective: Ga2O3 for ultra-high power rectifiers and MOSFETS, *J. Appl. Phys.* 124 (22) (2018) 220901. doi:10.1063/1.5062841.
- [4] A. M. Marconnet, M. A. Panzer, K. E. Goodson, Thermal conduction phenomena in carbon nanotubes and related nanostructured materials, *Rev. Mod. Phys.* 85 (2013) 1295–1326. doi:10.1103/RevModPhys.85.1295.
- [5] Q. Weng, S. Komiyama, L. Yang, Z. An, P. Chen, S.-A. Biehs, Y. Kajihara, W. Lu, Imaging of nonlocal hot-electron energy dissipation via shot noise, *Science* 360 (6390) (2018) 775–778. doi:10.1126/science.aam9991.
- [6] A. F. Ioffe, L. S. Stil’bans, E. K. Iordanishvili, T. S. Stavitskaya, A. Gelbtuch, G. Vineyard, Semiconductor Thermoelements and Thermoelectric Cooling, *Phys. Today* 12 (5) (1959) 42–42. doi:10.1063/1.3060810.
- [7] A. Bulusu, D. G. Walker, Review of electronic transport models for thermoelectric materials, *Superlattices Microstruct.* 44 (1) (2008) 1–36. doi:https://doi.org/10.1016/j.spmi.2008.02.008.
- [8] J. Ren, Geometric thermoelectric pump: Energy harvesting beyond seebeck and pyroelectric effects, *Chinese Phys. Lett.* 40 (9) (2023) 090501. doi:10.1088/0256-307X/40/9/090501.
- [9] L. Levitov, G. Falkovich, Electron viscosity, current vortices and negative nonlocal resistance in graphene, *Nat. Phys.* 12 (7) (2016) 672–676. doi:10.1038/nphys3667.
- [10] A. Aharon-Steinberg, T. Völkl, A. Kaplan, A. K. Pariari, I. Roy, T. Holder, Y. Wolf, A. Y. Meltzer, Y. Myasoedov, M. E. Huber, B. Yan, G. Falkovich, L. S. Levitov, M. Hücker, E. Zeldov, Direct observation of vortices in an electron fluid, *Nature* 607 (7917) (2022) 74–80. doi:10.1038/s41586-022-04794-y.
- [11] C. Kumar, J. Birkbeck, J. A. Sulpizio, D. Perello, T. Taniguchi, K. Watanabe, O. Reuven, T. Scaffidi, A. Stern, A. K. Geim, S. Ilani, Imaging hydrodynamic electrons flowing without Landauer–Sharvin resistance, *Nature* 609 (7926) (2022) 276–281. doi:10.1038/s41586-022-05002-7.
- [12] C. Tellier, A. Tossier, *Size Effects in Thin Films*, Elsevier, Amsterdam, 1982. doi:https://doi.org/10.1016/C2009-0-12632-6.
- [13] G. Chen, *Nanoscale energy transport and conversion: a parallel treatment of electrons, molecules, phonons, and photons*, Oxford University Press, 2005.
- [14] J. Callaway, Model for lattice thermal conductivity at low temperatures, *Phys. Rev.* 113 (1959) 1046–1051. doi:10.1103/PhysRev.113.1046.
- [15] M. Chandra, G. Kataria, D. Sahdev, R. Sundararaman, Hydrodynamic and ballistic ac transport in two-dimensional fermi liquids, *Phys. Rev. B* 99 (2019) 165409. doi:10.1103/PhysRevB.99.165409.
- [16] A. Gupta, J. J. Heremans, G. Kataria, M. Chandra, S. Fallahi, G. C. Gardner, M. J. Manfra, Hydrodynamic and ballistic transport over large length scales in GaAs/AlGaAs, *Phys. Rev. Lett.* 126 (2021) 076803. doi:10.1103/PhysRevLett.126.076803.

- [17] D. A. Bandurin, I. Torre, R. K. Kumar, M. B. Shalom, A. Tomadin, A. Principi, G. H. Auton, E. Khestanova, K. S. Novoselov, I. V. Grigorieva, L. A. Ponomarenko, A. K. Geim, M. Polini, Negative local resistance caused by viscous electron backflow in graphene, *Science* 351 (6277) (2016) 1055–1058. doi:10.1126/science.aad0201.
- [18] P. J. W. Moll, P. Kushwaha, N. Nandi, B. Schmidt, A. P. Mackenzie, Evidence for hydrodynamic electron flow in PdCoO<sub>2</sub>, *Science* 351 (6277) (2016) 1061–1064. doi:10.1126/science.aac8385.
- [19] J. Crossno, J. K. Shi, K. Wang, X. Liu, A. Harzheim, A. Lucas, S. Sachdev, P. Kim, T. Taniguchi, K. Watanabe, T. A. Ohki, K. C. Fong, Observation of the dirac fluid and the breakdown of the wiedemann-franz law in graphene, *Science* 351 (6277) (2016) 1058–1061. doi:10.1126/science.aad0343.
- [20] K. Bløtekjær, E. B. Lunde, Collision integrals for displaced maxwellian distribution, *Phys. Stat. Solidi (B)* 35 (2) (1969) 581–592. doi:https://doi.org/10.1002/pssb.19690350206.
- [21] K. Blotekjaer, Transport equations for electrons in two-valley semiconductors, *IEEE Trans. Electron. Devices* 17 (1) (1970) 38–47. doi:10.1109/T-ED.1970.16921.
- [22] R. Stratton, Semiconductor current-flow equations (diffusion and degeneracy), *IEEE Trans. Electron. Devices* 19 (12) (1972) 1288–1292. doi:10.1109/T-ED.1972.17592.
- [23] C. Jacoboni, L. Reggiani, The monte carlo method for the solution of charge transport in semiconductors with applications to covalent materials, *Rev. Mod. Phys.* 55 (1983) 645–705. doi:10.1103/RevModPhys.55.645.
- [24] W. Miao, Y. Guo, X. Ran, M. Wang, Deviatonal monte carlo scheme for thermal and electrical transport in metal nanostructures, *Phys. Rev. B* 99 (2019) 205433. doi:10.1103/PhysRevB.99.205433.
- [25] H. S. L. John C. Chai, S. V. Patankar, Ray effect and false scattering in the discrete ordinates method, *Numer. Heat Transfer B* 24 (4) (1993) 373–389. doi:10.1080/10407799308955899.
- [26] J. C. Huang, T. Y. Hsieh, J. Y. Yang, A conservative discrete ordinate method for solving semiclassical Boltzmann-BGK equation with Maxwell type wall boundary condition, *J. Comput. Phys.* 290 (2015) 112–131. doi:https://doi.org/10.1016/j.jcp.2015.02.037.
- [27] N. Goldsman, L. Henrickson, J. Frey, A physics-based analytical/numerical solution to the Boltzmann transport equation for use in device simulation, *Solid-State Electron.* 34 (4) (1991) 389–396. doi:https://doi.org/10.1016/0038-1101(91)90169-Y.
- [28] A. Gnudi, D. Ventura, G. Baccarani, One-dimensional simulation of a bipolar transistor by means of spherical harmonics expansion of the boltzmann transport equation, in: W. Fichtner, D. Aemmer (Eds.), *Proceedings of SISDEP*, Vol. 4, 1991, pp. 205–213.
- [29] K. Rahmat, J. White, D. Antoniadis, Simulation of semiconductor devices using a galerkin/spherical harmonic expansion approach to solving the coupled poisson-boltzmann system, *IEEE Trans. Comput. Aided Des. Integr. Circuits Syst.* 15 (10) (1996) 1181–1196. doi:10.1109/43.541439.
- [30] K. A. Hennacy, Y. J. Wu, N. Goldsman, I. D. Mayergoyz, Deterministic MOSFET simulation using a generalized spherical harmonic expansion of the Boltzmann equation, *Solid-State Electron.* 38 (8) (1995) 1485–1495. doi:https://doi.org/10.1016/0038-1101(94)00280-S.
- [31] K. Rupp, A. Jüngel, T. Grasser, Matrix compression for spherical harmonics expansions of the Boltzmann transport equation for semiconductors, *J. Comput. Phys.* 229 (23) (2010) 8750–8765. doi:https://doi.org/10.1016/j.jcp.2010.08.008.
- [32] Z. Guo, C. Shu, *Lattice Boltzmann method and its application in engineering*, Vol. 3, World Scientific, 2013.
- [33] A. Chattopadhyay, A. Pattamatta, A comparative study of submicron phonon transport using the boltzmann transport equation and the lattice boltzmann method, *Numer. Heat Transfer B* 66 (4) (2014) 360–379. doi:10.1080/10407790.2014.915683.
- [34] Z. Guo, K. Xu, R. Wang, Discrete unified gas kinetic scheme for all knudsen number flows: Low-speed isothermal case, *Phys. Rev. E* 88 (2013) 033305. doi:10.1103/PhysRevE.88.033305.
- [35] Z. Guo, R. Wang, K. Xu, Discrete unified gas kinetic scheme for all knudsen number flows. ii. thermal compressible case, *Phys. Rev. E* 91 (2015) 033313. doi:10.1103/PhysRevE.91.033313.
- [36] Z. Guo, K. Xu, Progress of discrete unified gas-kinetic scheme for multiscale flows, *Adva. Aerodyn.* 3 (1) (2021) 6. doi:10.1186/s42774-020-00058-3.
- [37] C. Zhang, R. Guo, M. Lian, J. Shiomi, Electron-phonon coupling and non-equilibrium thermal conduction in ultrafast heating systems (2023). arXiv:2305.06567.
- [38] K. E. Nagaev, O. S. Ayvazyan, Effects of electron-electron scattering in wide ballistic microcontacts, *Phys. Rev. Lett.* 101 (2008) 216807. doi:10.1103/PhysRevLett.101.216807.
- [39] C. Hua, A. J. Minnich, Semi-analytical solution to the frequency-dependent Boltzmann transport equation for cross-plane heat conduction in thin films, *J. Appl. Phys.* 117 (17) (2015) 175306. doi:10.1063/1.4919432.
- [40] K. Fuchs, The conductivity of thin metallic films according to the electron theory of metals, *Math. Proc. Camb. Phil. Soc.* 34 (1938) 100–108.
- [41] E. Sondheimer, The mean free path of electrons in metals, *Adv. Phys.* 1 (1) (1952) 1–42. doi:10.1080/00018735200101151.
- [42] M. Battiato, V. Zlatic, K. Held, Boltzmann approach to high-order transport: The nonlinear and nonlocal responses, *Phys. Rev. B* 95 (2017) 235137. doi:10.1103/PhysRevB.95.235137.
- [43] P. B. Allen, M. Liu, Joule heating in boltzmann theory of metals, *Phys. Rev. B* 102 (2020) 165134. doi:10.1103/PhysRevB.102.165134.